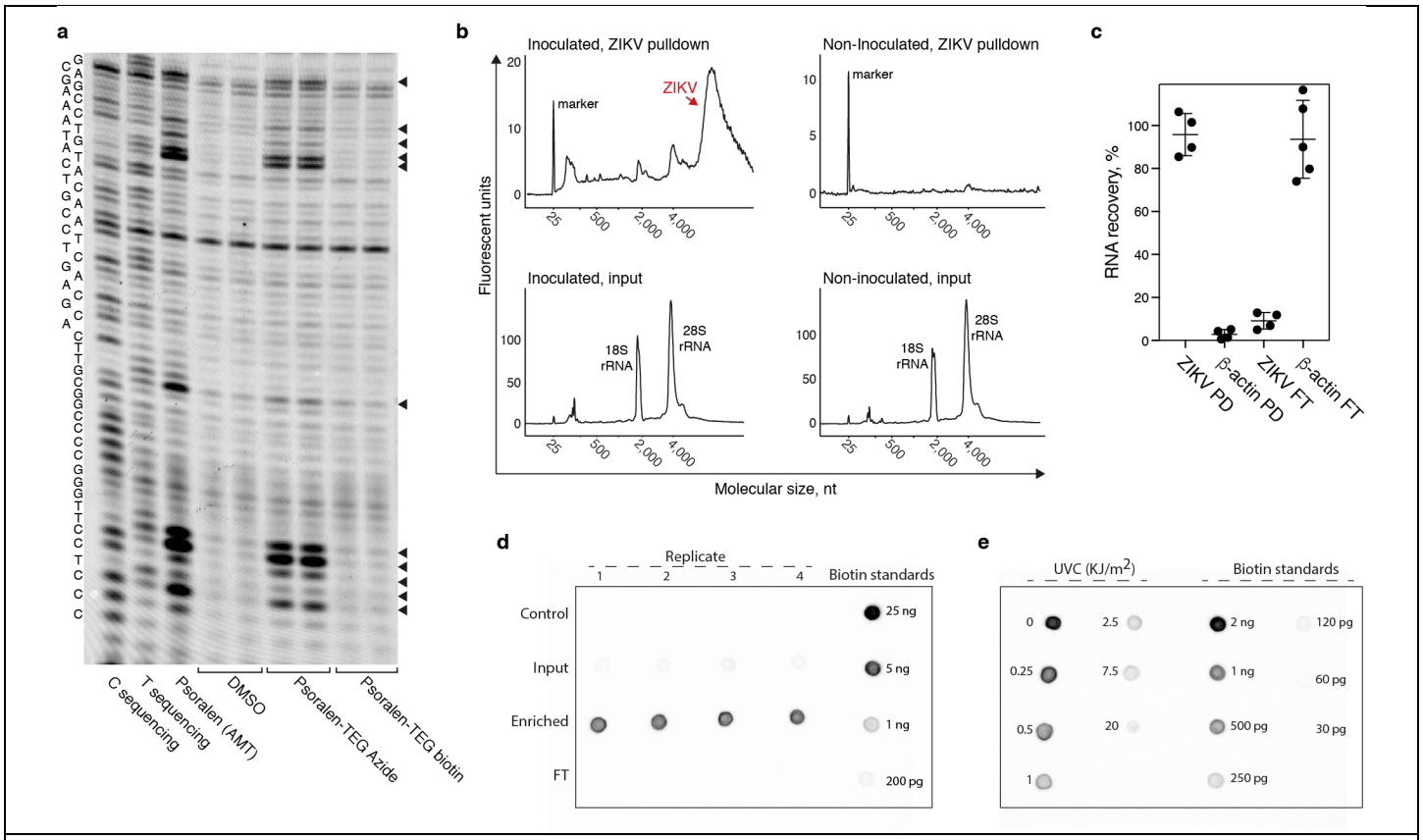

Supplementary Figure 1

COMRADES assay development

a, Reverse transcription stalling assay indicating *in vivo* crosslinking positions in the human 5.8S rRNA from cells treated with the indicated psoralen derivative. Arrows indicate stalling events; Sequence is shown to the left. b, Bioanalyzer RNA profiles of ZIKV enriched or input RNA from cells inoculated with ZIKV or control non-inoculated cells. c, Enrichment of ZIKV RNA, or a control β-actin RNA measured by TaqMan PCR. Mean and s.d. of 4-5 biologically independent samples is shown. d-e, Non-cropped dot-blots showing enrichment of crosslinked RNA (d) or crosslink reversal (e). FT: flow through; Control: non-crosslinked sample; UVC: short wavelength UV. Experiments were repeated independently 3 times (a-e) with similar results.

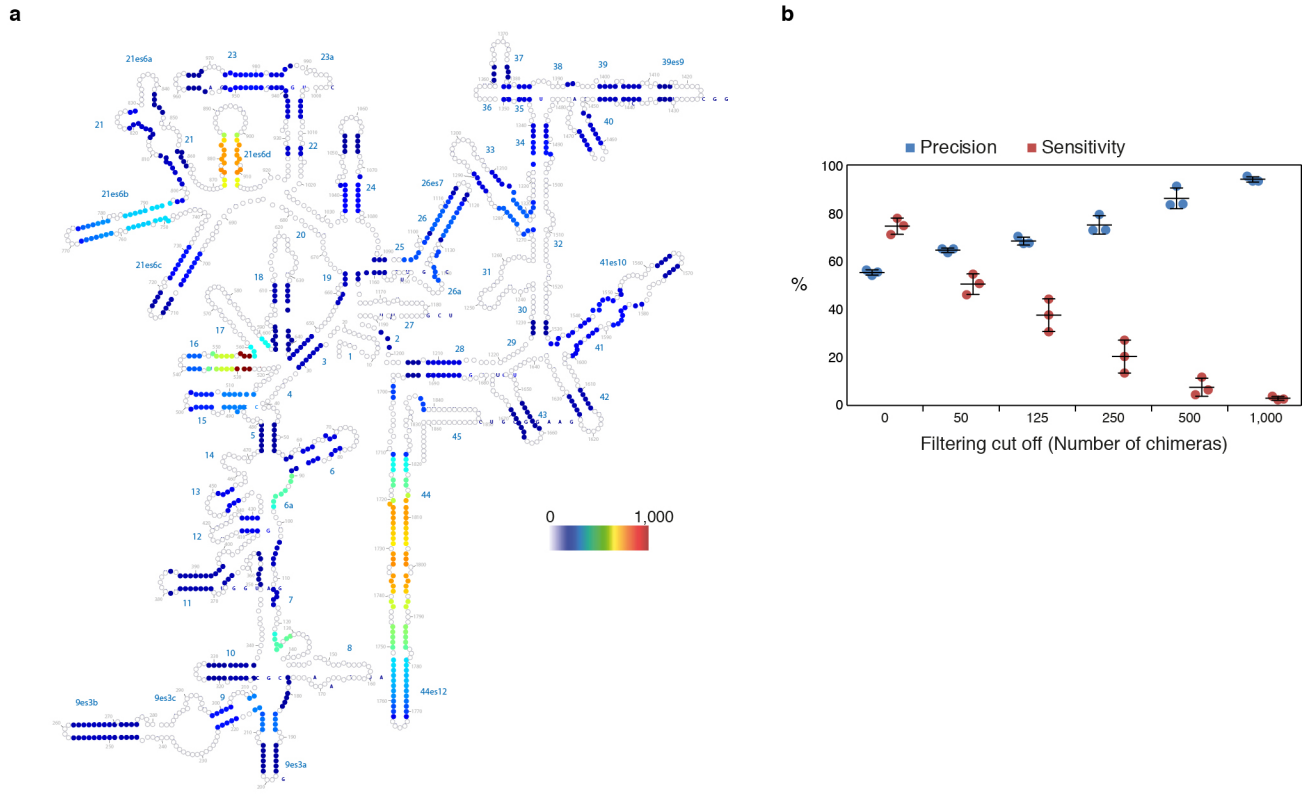

Supplementary Figure 2

COMRADES validation

a, *In vivo* detected interactions overlaid on the Ribovision human 18S phylogenetic ribosomal RNA secondary structure. Colour-code is indicative of the number of supporting chimeras for each base-pair. b, Precision and sensitivity of ribosomal RNA base-pairing detection by COMRADES. Mean and s.d. of 3 independent experiments are shown. Analysis is based on ZIKV enriched libraries, therefore the sensitivity of COMRADES is expected to be underestimated by this analysis.

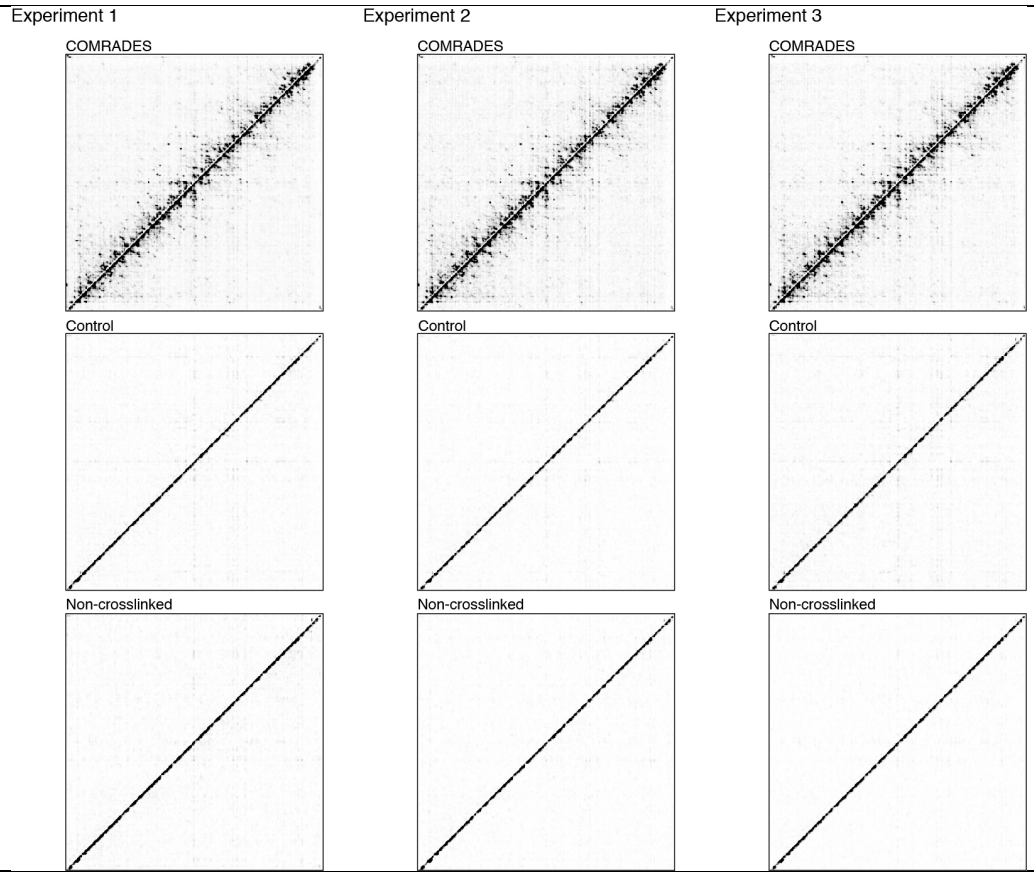

Supplementary Figure 3

Intra-viral RNA interactions

Heat maps of ZIKV RNA-RNA interactions in crosslinked libraries and controls. Chimeras ligated in 5'-3' and 3'-5' orientations are plotted above and below the diagonal respectively. Experiments 1-3 represent independent experiments carried out at different days.

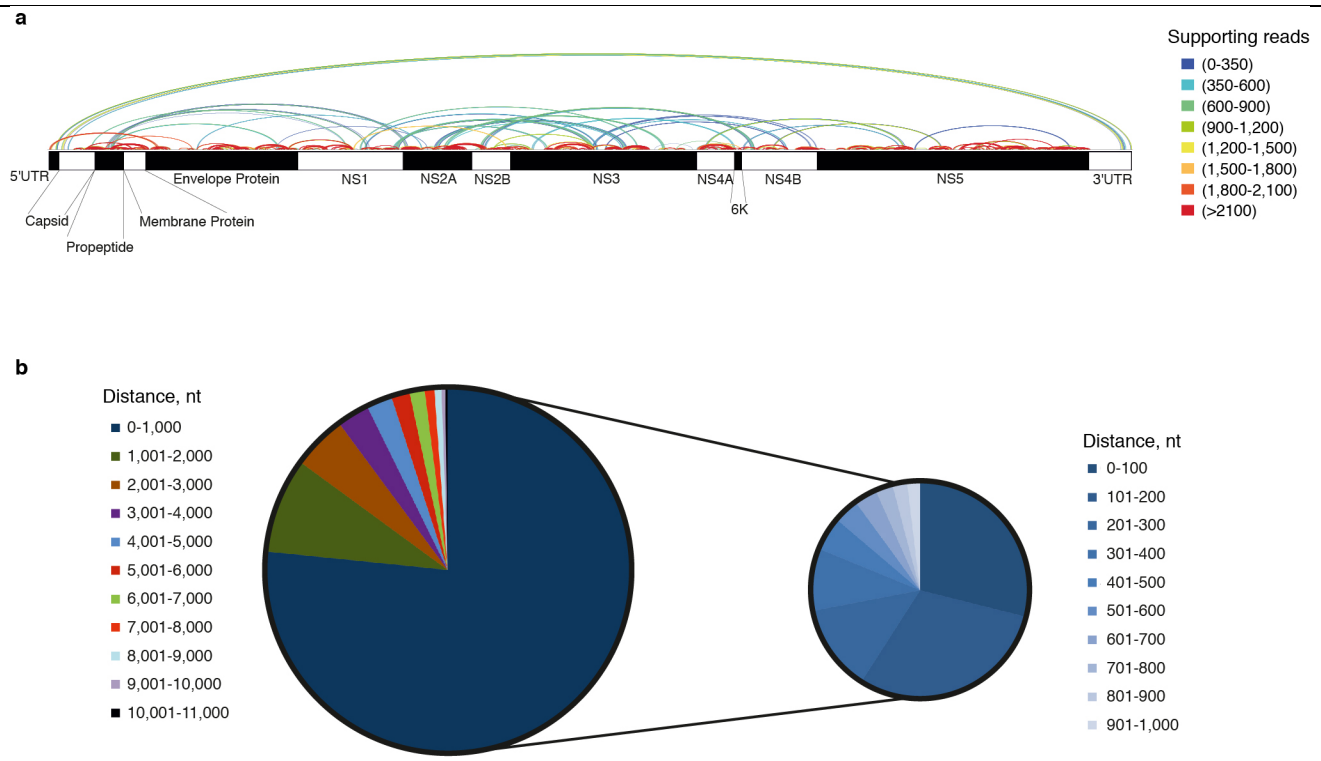

Supplementary Figure 4

Short- and long-range RNA-RNA interactions along the ZIKV genome

a, Arch plot representation of short and long-range RNA-RNA interactions along the ZIKV genome. Colours representing the number of non-redundant chimeric reads supporting each interaction. b, Distribution of RNA-RNA interactions by nucleotide distance between interacting chimeric partners. Left pie chart shows distribution of all interactions; right pie chart shows distribution of interactions that span less than 1,000 nucleotides.

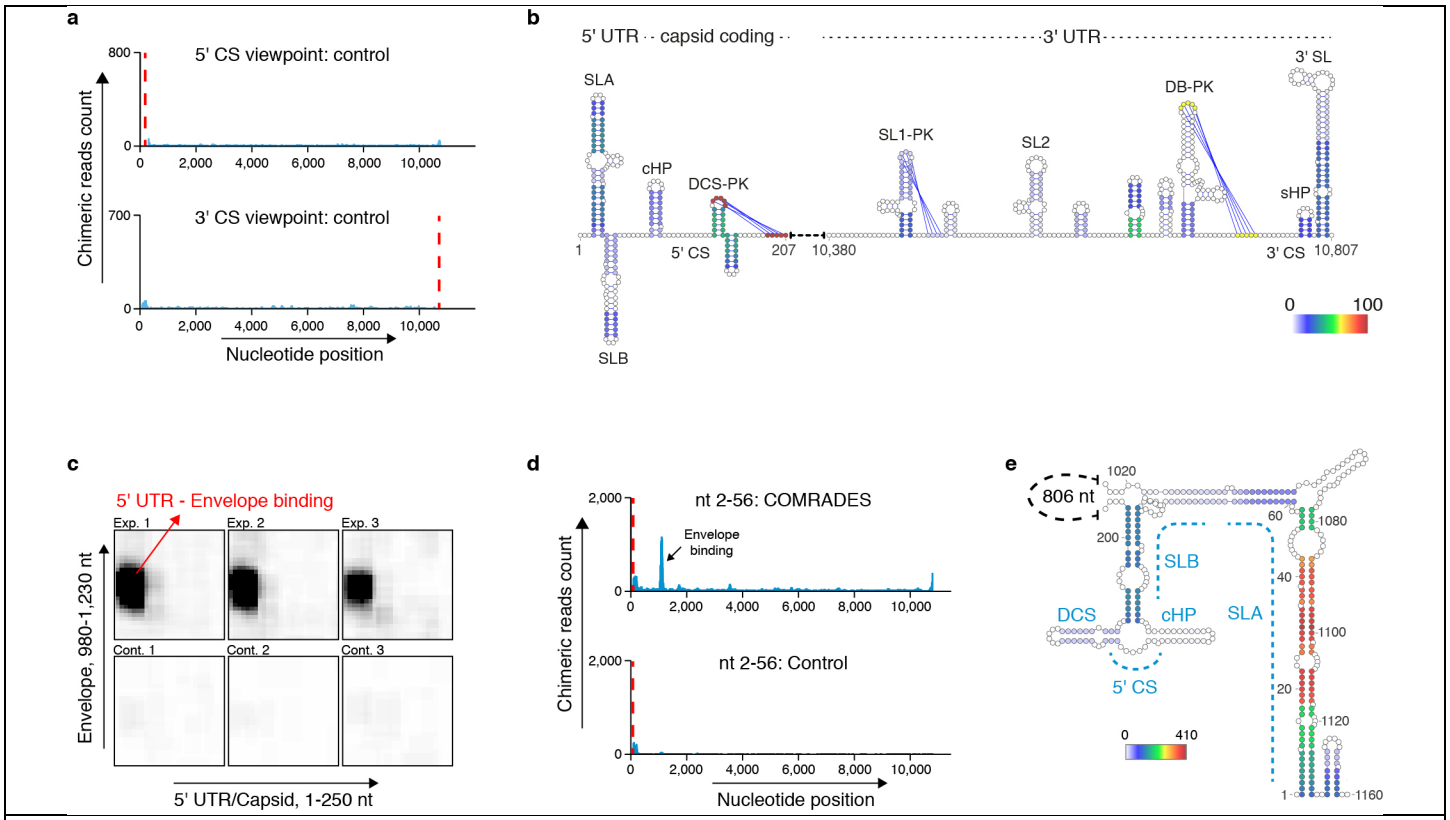

Supplementary Figure 5

The genomic structure of ZIKV inside human cells

a, Viewpoint histograms showing binding positions of the cyclization sequences along the ZIKV genome in control libraries; related to Fig. 2b. Viewpoint regions are marked by dashed red lines. b, The non-circular ZIKV genome conformation. Color code is indicative of the number of supporting chimeras for each base-pair. c, Heatmap of RNA-RNA interactions between the 5' UTR and the envelope coding region. d, Viewpoint histogram showing binding of nucleotides at position 2-56 along the ZIKV genome. e, Newly identified 5' UTR structure. Color code as described in (b).

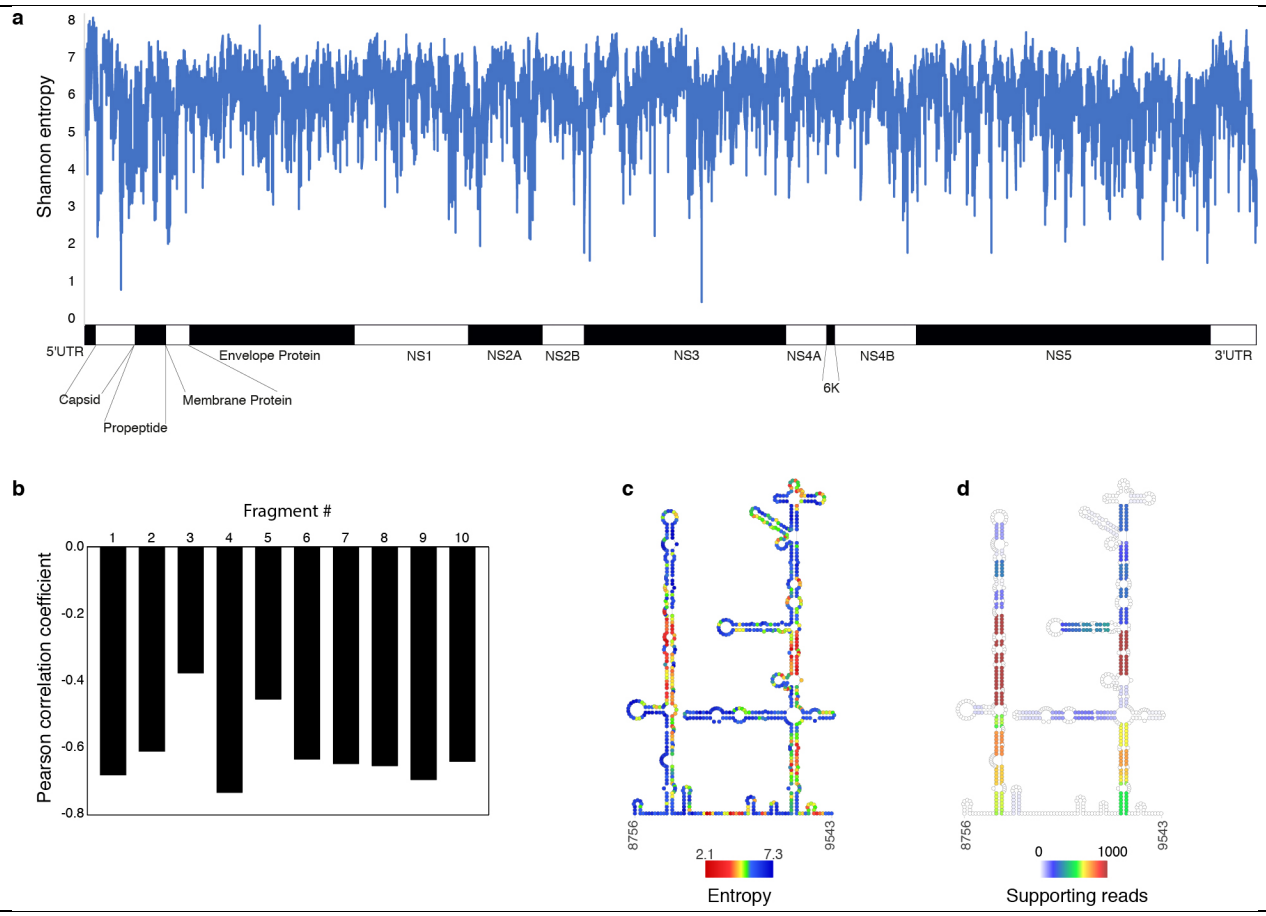

Supplementary Figure 6

Folding entropy

a, Shannon entropy values calculated for each nucleotide along the ZIKV genome. Entropy may range from 0 to 13.4 bits; ZIKV coordinates are indicated by the position of genomic elements below. b, Inverse correlation between the degree of experimental support of base paired regions and their entropy. Pearson correlation coefficient values were calculated for each 1,000 structures. c, Shannon entropy values for a selected region of the ZIKV genome. d, Number of supporting chimeric reads for each base-pair shown in (c).

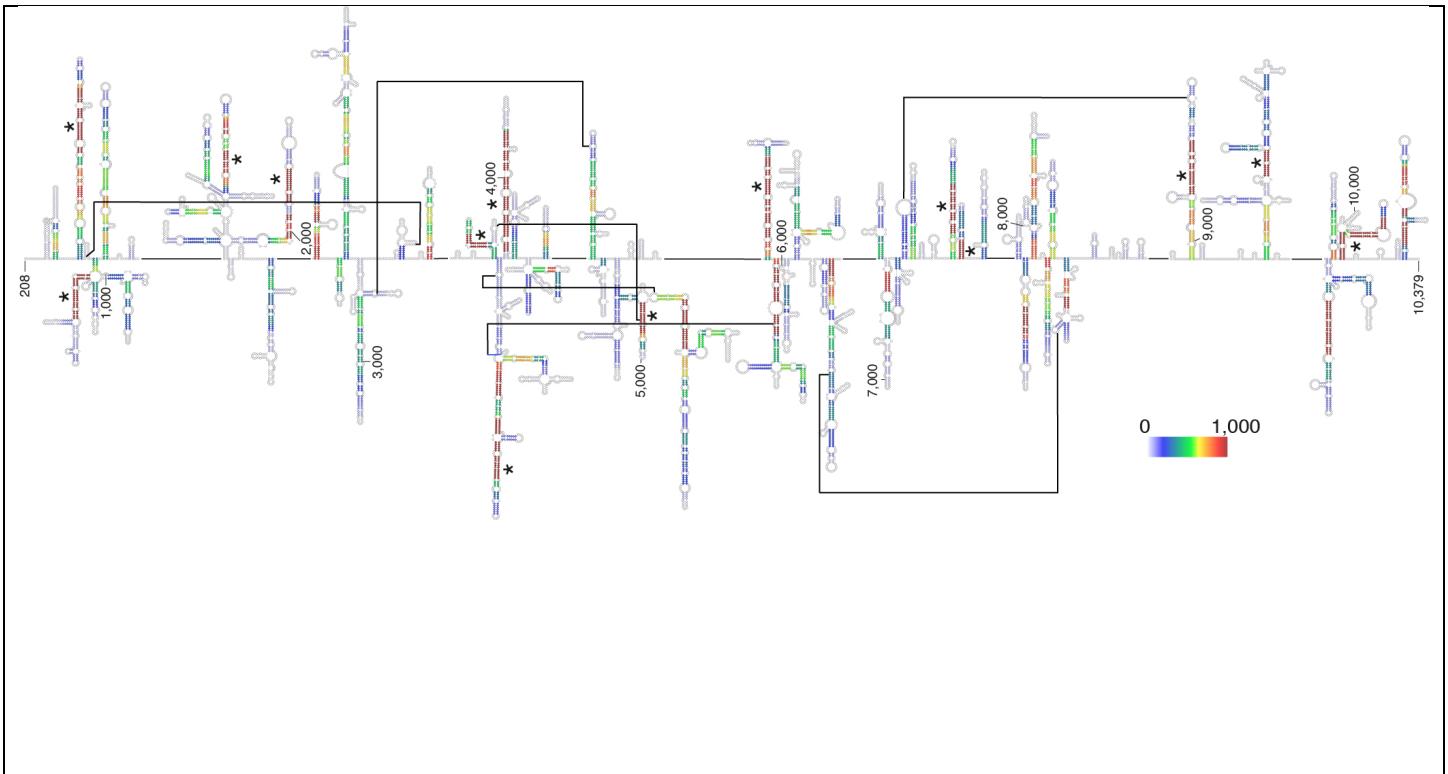

Supplementary Figure 7

Low Shannon entropy regions along the ZIKV coding region

The ZIKV genome conformation with the highest chimeric-reads support. Color code is indicative of the number of supporting chimeras for each base-pair. *: Regions with exceptionally low Shannon entropy; Vertical lines indicate long-distance interactions

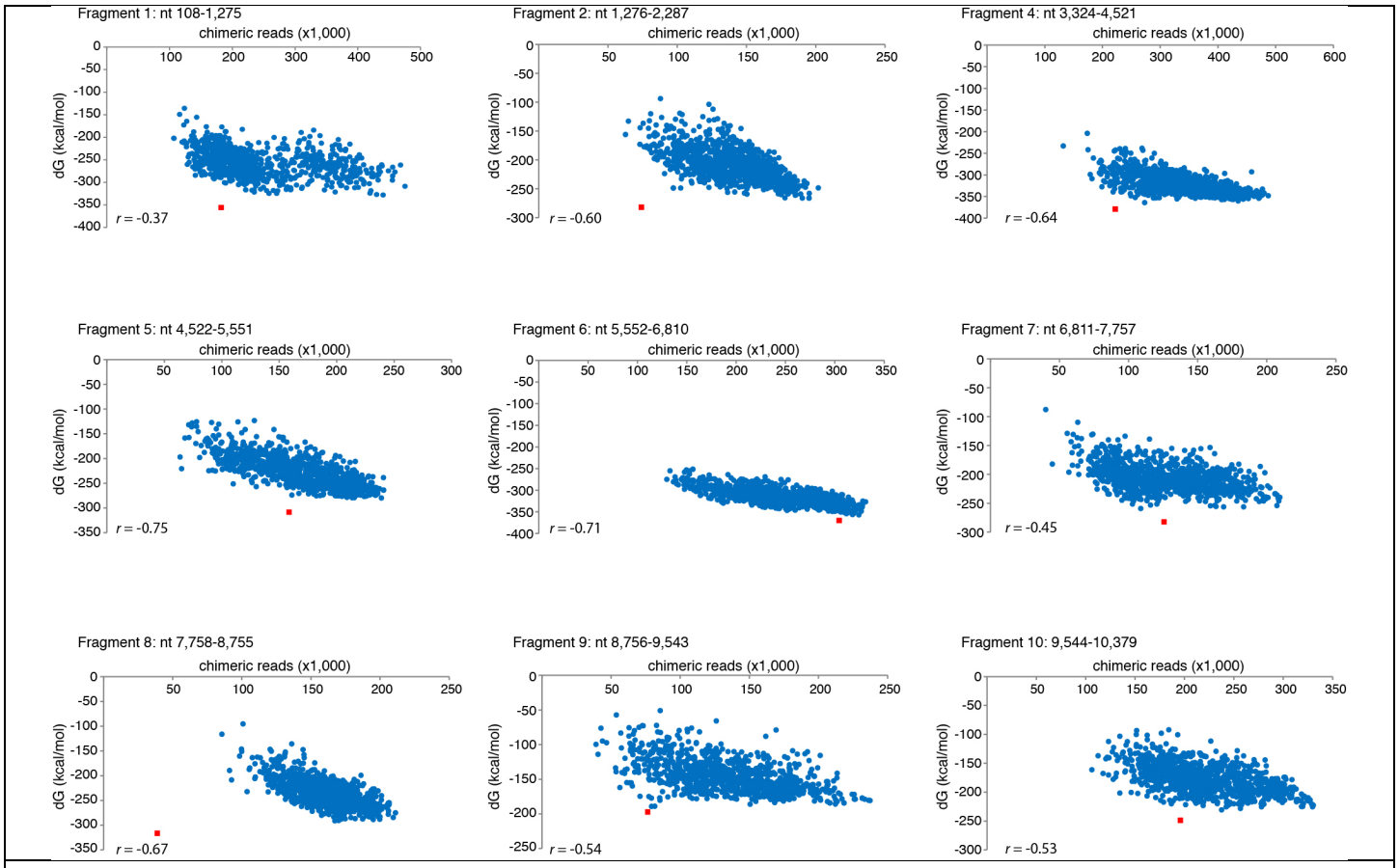

Supplementary Figure 8

Randomized parallel RNA folding

Computationally predicted structures for ~1,000 nucleotides regions along the ZIKV genome, related to Fig. 2d. Each structure is plotted as a dot according to its folding energy (dG) and experimentally supporting evidence (chimera reads). Red dots indicating the structure with the lowest possible folding energy for each region. *r*: Pearson correlation coefficient.

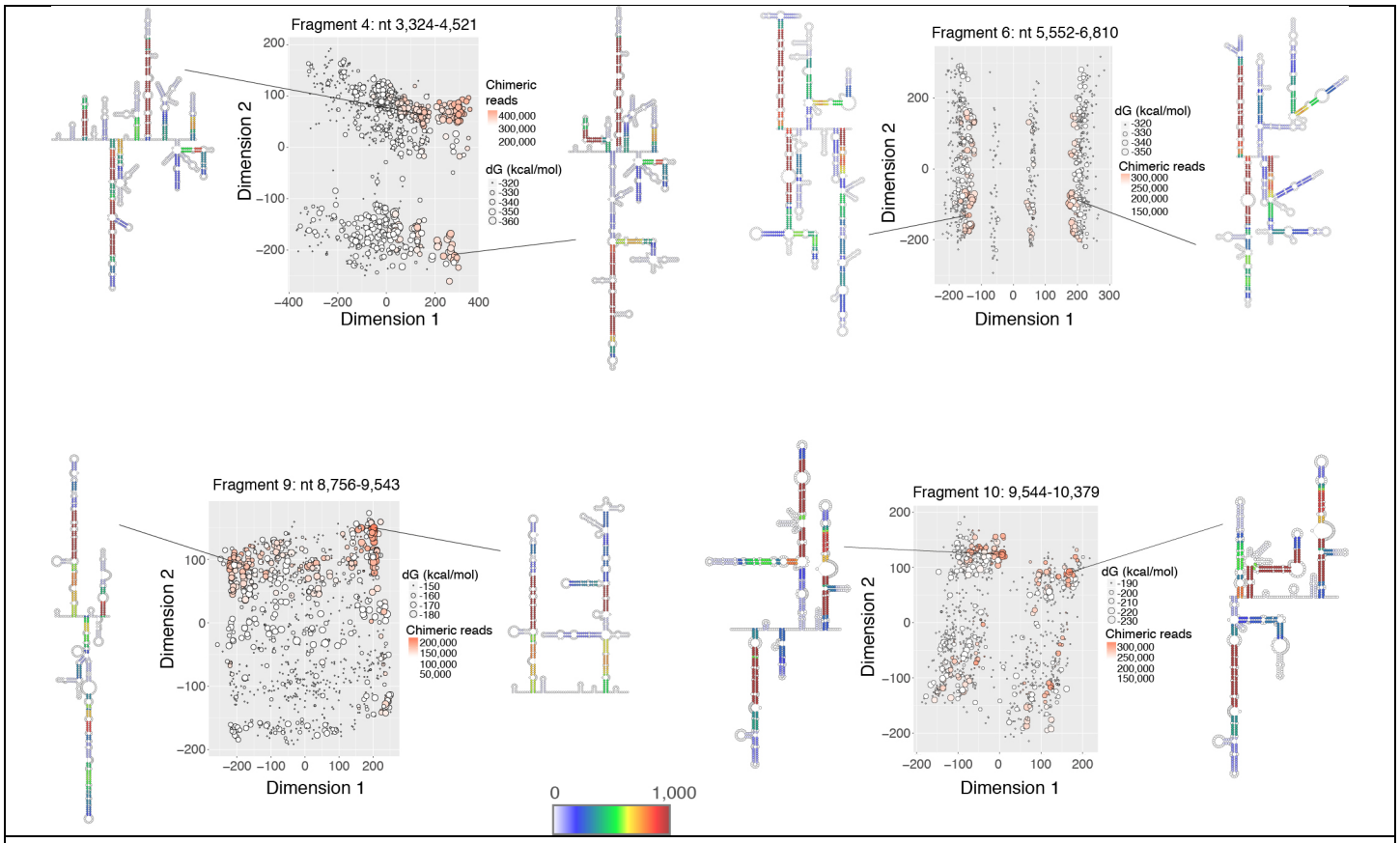

Supplementary Figure 9

Clustering of structures

Clustering of structures based on degree of similarity, related to Fig. 2e. Example of structures are shown with a color code representing the number of non-redundant chimeric reads supporting each interaction. Only regions demonstrating a clear clustering pattern are shown.

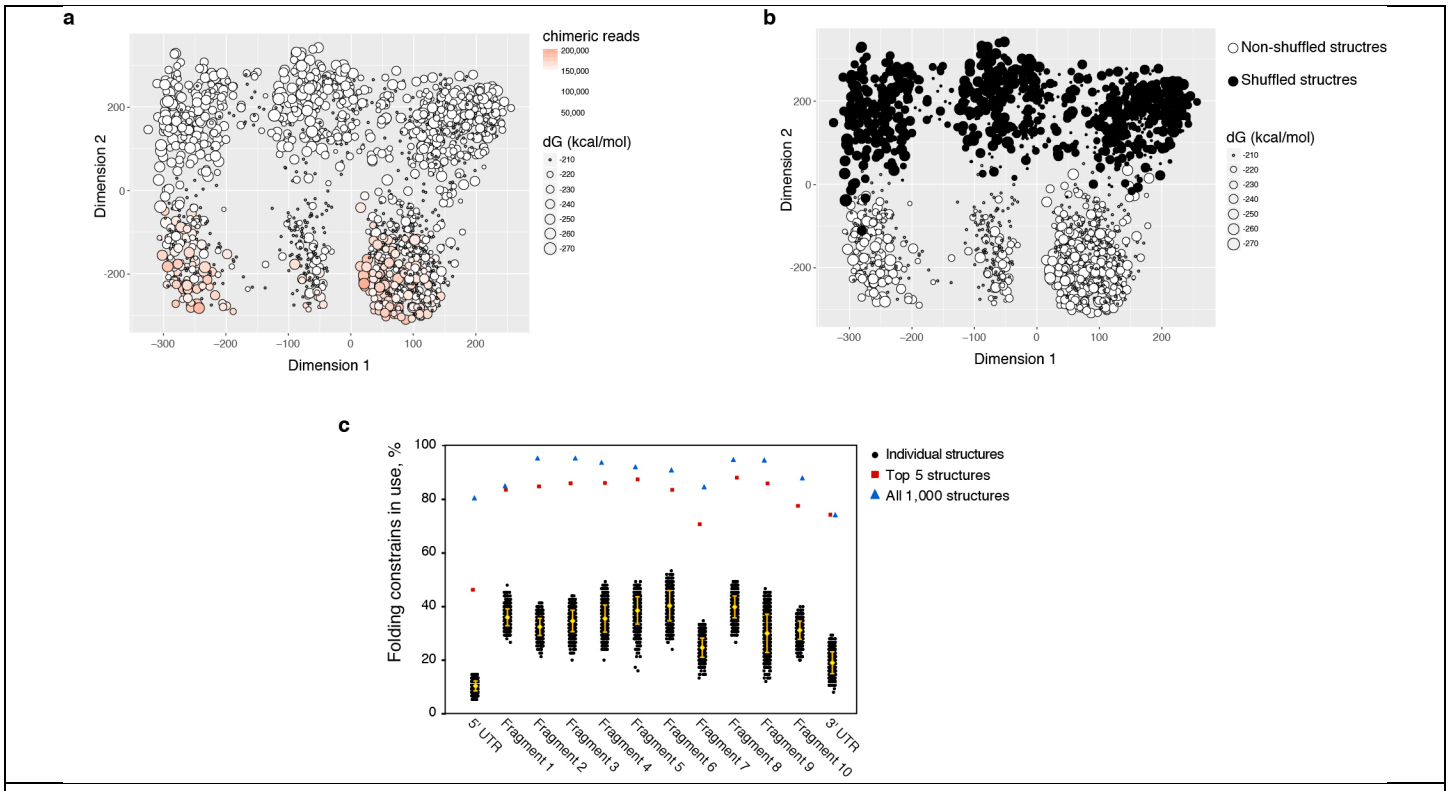

Supplementary Figure 10

Ensemble of coexisting structures

a-b, Co-clustering of non-shuffled and shuffled structures, related to Fig. 2e. Red scale indicates the number of chimeric reads supporting each non-shuffled structure (a). c, Representation of the percent of *in vivo* probed interactions in use in an ensemble of 5 structures per region, an ensemble of all 1,000 structures per region, or individual structures. Yellow lines represent mean and s.d. of 1,000 structures.

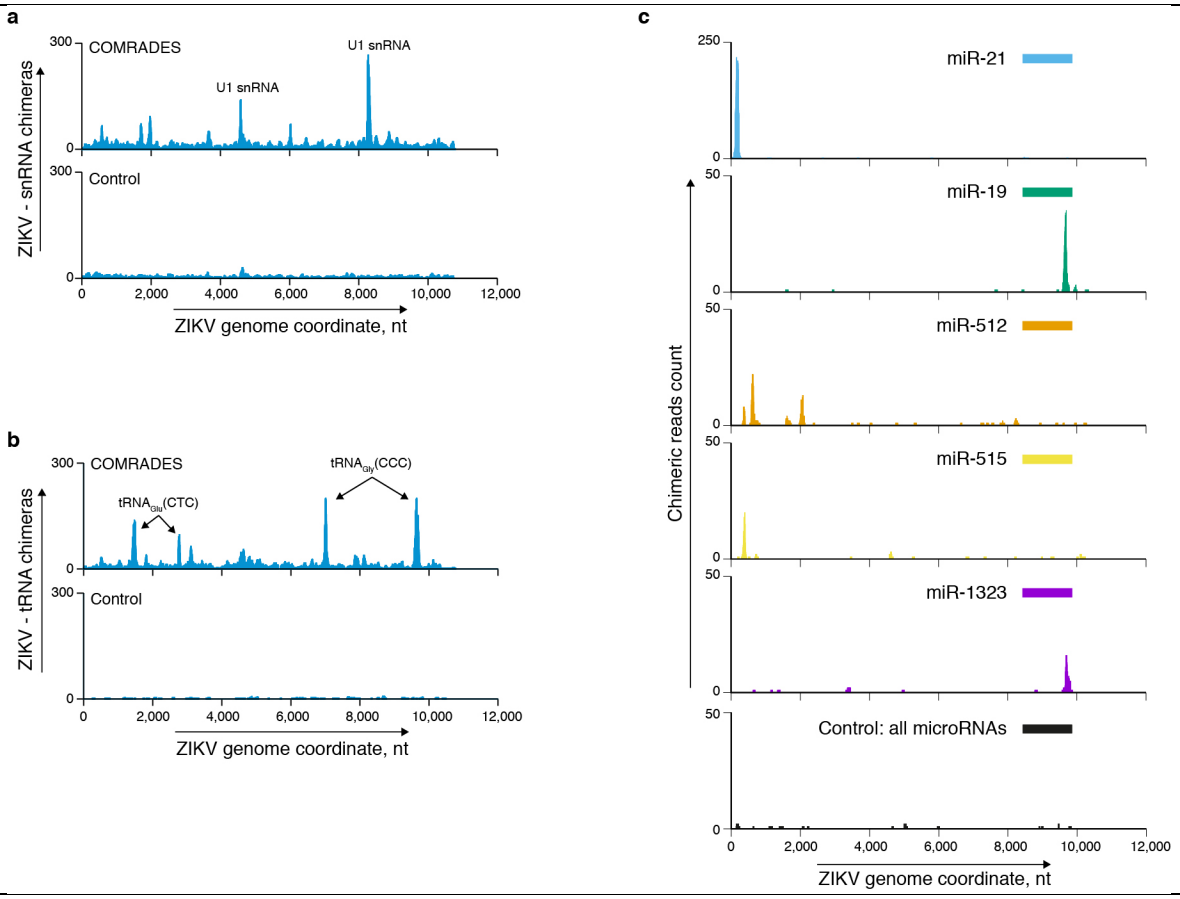

Supplementary Figure 11

Insert figure title here by deleting or overwriting this text; keep title to a single sentence.

a-c, Site specific base-pairing between the ZIKV genome and small nuclear RNAs (a), tRNAs (b) and specific miRNAs (c) in COMRADES and controls.

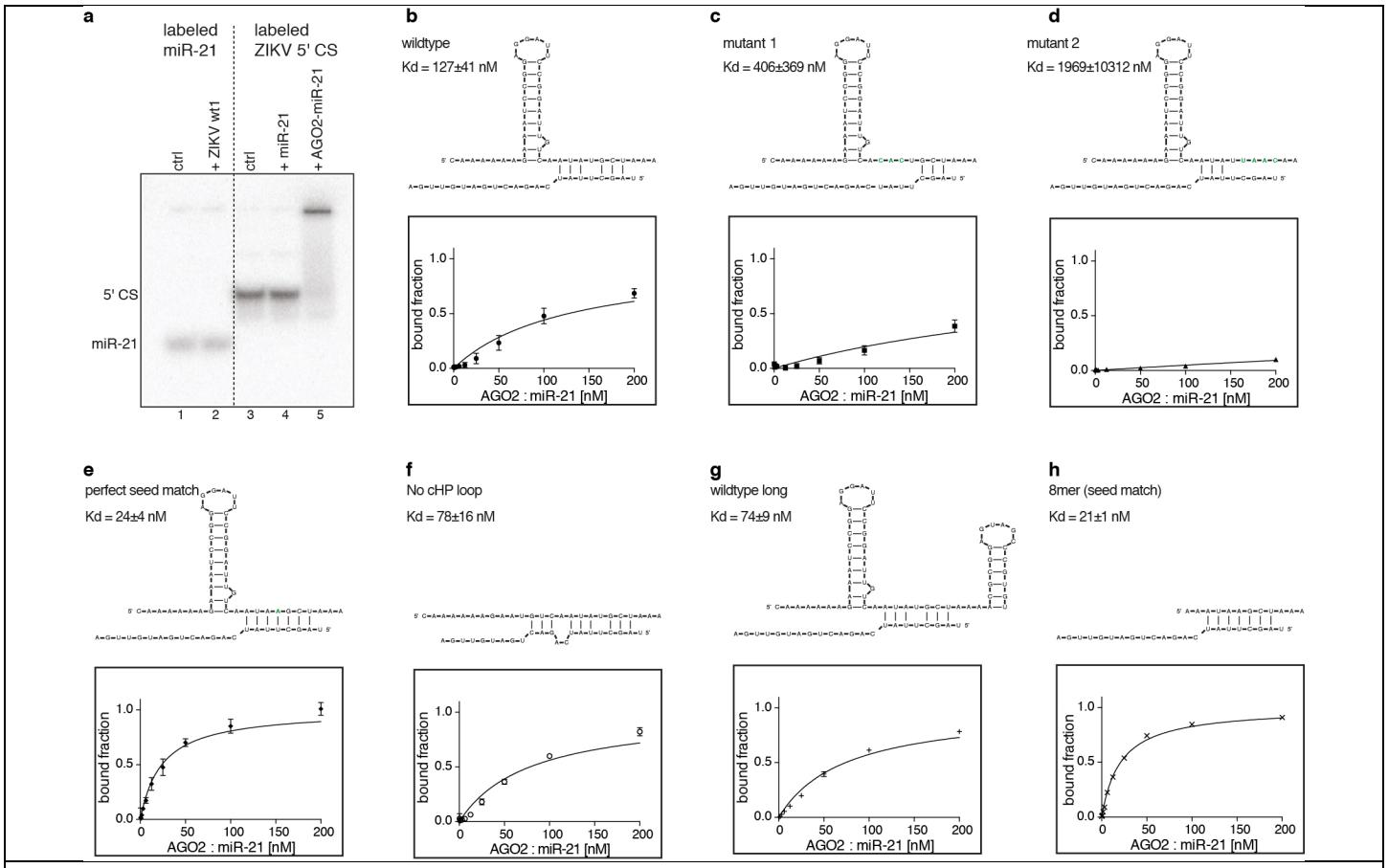

Supplementary Figure 12

In vitro affinity of Ago2-miR-21 to the ZIKV 5' CS

a, Electrophoretic mobility shift assay (EMSA) of 5'-labeled miR-21 (lanes 1, 2) upon addition of ZIKV 5' CS (lane 2); and 5'-labeled ZIKV 5' CS (lanes 3-5) upon addition of miR-21 (lane 4) or of Ago2-miR-21 complexes. The experiment was independently repeated 3 times with similar results (lane 5). b-h, *In vitro* measured affinities of Ago2-miR-21 to a wildtype ZIKV 5' CS. Mean and s.e.m. of 3 independent samples are shown. (b), mutated 5' CS (c-d), a fully seed matched mutated 5' CS (e), mutated 5' CS with no cHP stem-loop (f), extended 5' CS sequence containing the DCS stem-loop (g), and a short target perfectly complementary to the miR-21 seed (h).

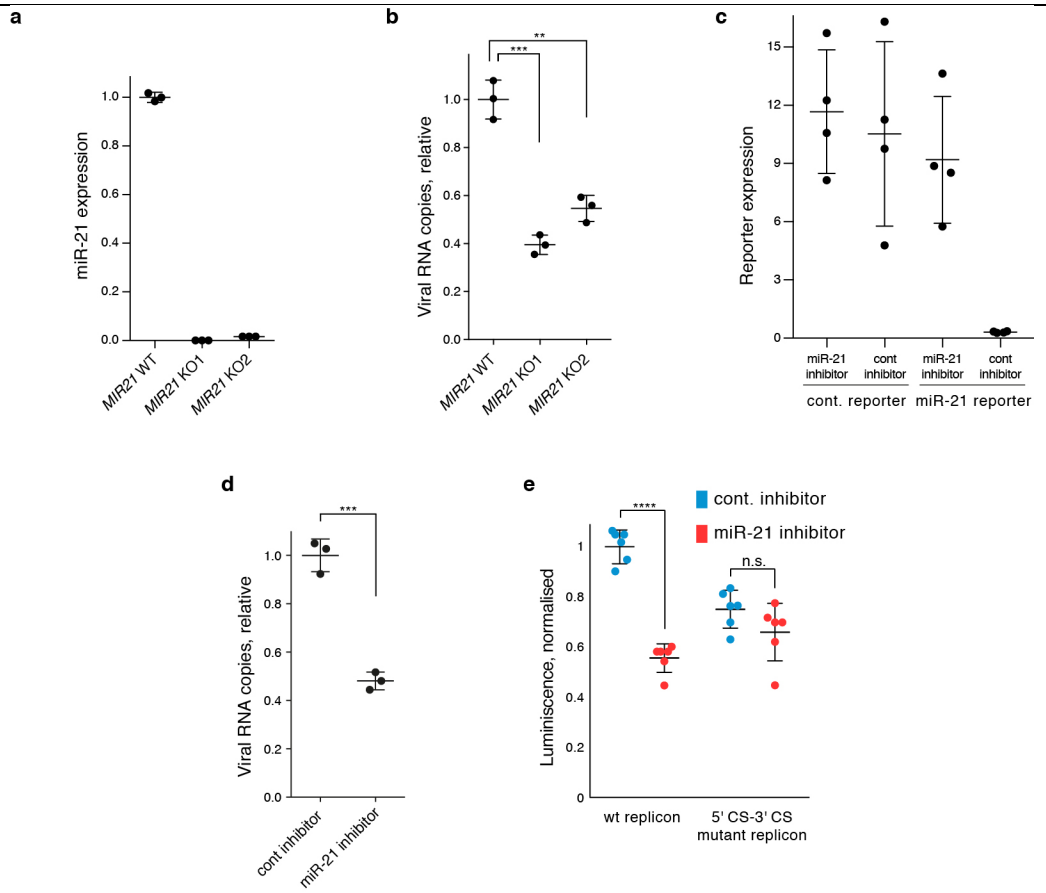

Supplementary Figure 13

miR-21 affects ZIKV RNA production

a, TaqMan PCR measurements of mature miR-21 expression levels in wildtype cells and CRISPR/Cas9 *MIR21* deletion-clones. Values are normalized to spike-in control. b, Intracellular ZIKV RNA in *MIR21* knockout and wildtype cells. Two-sided Student's t-test p-values: ** =0.001; *** =0.0002, 4 degrees of freedom. c, Expression level of control and miR-21 psiCHECK-2 reporters upon treatment with miR-21 or control inhibitors. miR-21 expression values denote for Renilla / Firefly luminescence signals. d, Intracellular ZIKV RNA in miR-21 inhibited and control cells. Two-sided Student's t-test p-value: *** =0.0003, 4 degrees of freedom. e, Replication of a ZIKV replicon carrying a wildtype 5' CS or a 5' CS - 3' CS double mutant, pre-treated with miR-21 or non-targeting inhibitors. Two-sided Student's t-test p-values: **** =3.5E-07; n.s.= 0.1 (non-significant), 10 degrees of freedom. wt: wildtype; KO: CRISPR-Cas9 *MIR21* deletion-clones; cont: control. Mean and s.d. of 3 (a, b, d), 4 (c), and 6 (e) biologically independent samples are shown.

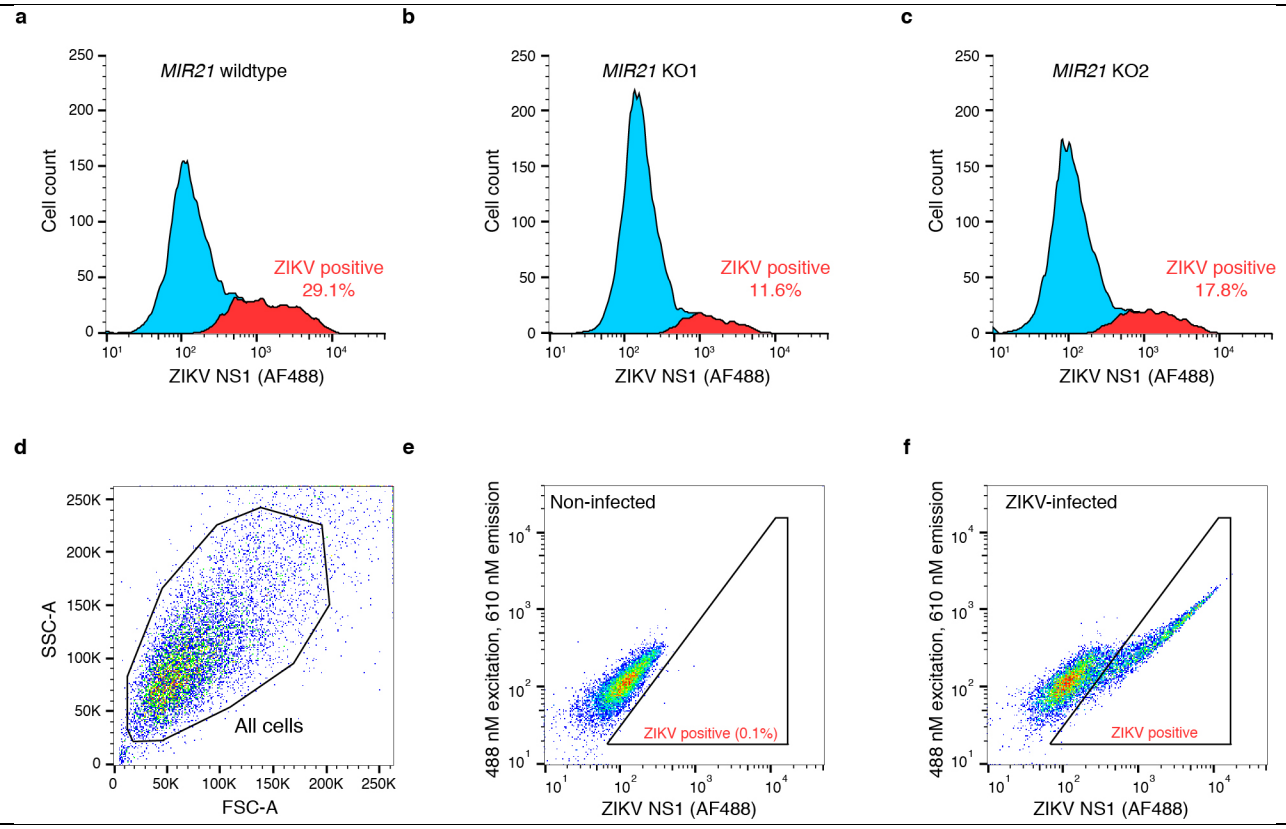

Supplementary Figure 14

miR-21 affects ZIKV protein production

a-c, Intracellular levels of ZIKV envelope protein (ZIKV NS1), measured by FACS. Representative experiment out of 3 is shown. d-f, Gating strategy for the FACS measurements shown in (a-c). AF488: Alexa Fluor 488 labelled secondary antibody.